Supplement of Atmos. Chem. Phys., 23, 10795–10807, 2023
https://doi.org/10.5194/acp-23-10795-2023-supplement

Atmospheric Chemistry and Physics Open Access

Supplement of

Exploring the amplified role of HCHO in the formation of HMS and O_3 during the co-occurring $PM_{2.5}$ and O_3 pollution in a coastal city of southeast China

Youwei Hong et al.

Correspondence to: Youwei Hong (ywhong@iue.ac.cn) and Likun Xue (xuelikun@sdu.edu.cn)

The Observation-based model (OBM)

A chemical box model, as one of the important methods for analyzing atmospheric chemical processes, was run based on the platform of the Framework for 0-Dimensional Atmospheric Modeling (F0AM), which has broad application potential in deeply exploring atmospheric observation data and comprehensively understanding the regional atmospheric pollution. About the chemical mechanism, the F0AM incorporating the latest chemical mechanism version of MCM-v3.3.1 (MCM, http://mcm.leeds.ac.uk/MCM/, last access: 13 May 2022) was applied to simulate the detailed photochemical processes and quantify the reaction rates of HCHO mechanism, and the MCM mechanism introduced 142 VOCs and about 20,000 chemical reactions.

About the uncertainties of the model simulation results, the index of agreement (IOA) was used to judge the reliability of the model simulation results, as follows:

$$IOA = 1 - \frac{\sum_{i=1}^{n}(O_i - S_i)^2}{\sum_{i=1}^{n}(|O_i - \bar{O}| - |S_i - \bar{O}|)^2}$$

where *Si* is simulated value, *Oi* represents observed value, $\bar{O}$ is the average observed values, and n is the sample number. The IOA range is 0-1, and the higher the IOA value is, the better agreement between simulated and observed values is. In this study, the simulation results (the IOA is approximately 0.80) are reasonable, and the performance of the OBM-MCM model was acceptable.

Uncertainty evaluation of OBM analysis:

Since aqueous HCHO was not available during the observation, which was the key chemical components influencing the subsequent HMS modeling, we established the aqueous HCHO concentrations by the mass transfer processed between the gas- and particle- phase. Among this processes, the uncertainties were introduced somehow by the Henry's law constant adopted in the model. We conducted a sensitivity test with 2 folds of current used Henry's law constant of HCHO, with a value of 6×10^7 M atm^{-1}. As shown in Fig S0, the modeled aqueous HCHO as well as HMS concentrations increased with the increase of Henry's law constant in the sensitivity case, with increase of 0.01 and 0.13 μg m^{-3} for aqueous HCHO and HMS, respectively. It is quite reasonable considering the increased solubility of HCHO. On the other hand, the modeled HCHO and HMS were still exhibited higher concentrations during the pollution episodes (EP1 and EP2), of which higher precursors and favorable aerosol properties enhanced the heterogeneous processes. Therefore, the impacts of HCHO Henry's law constant approximations on the conclusions are supposed to be minor.

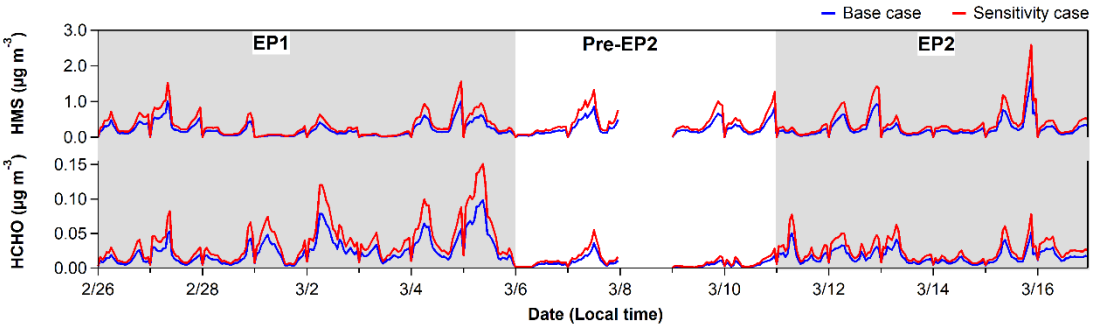

Fig S1. Time series of the modeled aqueous HCHO and HMS concentrations with the model used Henry's law constant of HCHO (referred as base case, the blue line) and 2 folds of the model used Henry's law constant of HCHO (referred as sensitivity case, the red line), respectively.

In the atmosphere, gaseous HCHO with high Henry's law constant can partition into aerosol or cloud/fog water, then the aqueous HCHO can reacts with H_2O_2 to form HMHP, with an upper bound forward rate constant of 100 (±35) M^{-1} s^{-1} and reverse rate constant of 0.6 (±0.2) s^{-1}(Dovrou et al.,2022). In the gas phase, HMHP is mainly formed by the hydration of CH_2OO Criegee radicals and then can partition into aerosol water, which have the potential to oxidize SO_2(aq) to form sulfate. From the perspective of contributions of HMHP paths to sulfate formation, the researcher revealed that the HCHO-catalysis path (HCHO + H_2O_2) under fast equilibrium is more significant than HMHP-direct path (hydration of CH2OO in the gas-phase) to global sulfate, so HCHO-catalysis path is significant for HMHP production. So, in the future, we will carry out the observation of H_2O_2 for further evaluate the effects of HCHO + H_2O_2 reaction on the HMHP production.

We used 2 folds of the HCHO Henry's law constant as the sensitivity case and conducted the simulation of the aqueous HCHO as well as HMS concentrations. We found that aqueous HCHO and HMS exhibited slight higher concentrations due to the increased solubility of HCHO, with increases of 0.01 and 0.13 μg m^{-3} for HCHO and HMS, respectively. However, the modeled HCHO and HMS were still exhibited higher concentrations during the pollution episodes (EP1 and EP2), which still able to support our major conclusions. On the other hand, we compared our modeling aqueous HCHO concentrations with previous observations. As shown in the following tables, our modeling aqueous HCHO concentrations are comparable and in the same order of magnitude with previous observations. Therefore, uncertainties due to the lack of aqueous HCHO measurement and the HCHO Henry's law constant approximations would take minor impacts on our major conclusions.

Backward trajectory analysis

Hybrid Single-Particle Lagrangian Integrated Trajectory (HYSPLIT) was used to analyze the air masses before and during the $PM_{2.5}$ and O_3 pollution period. Meteorological data used here were obtained from the Global Data Assimilation System (GDAS) with a 1°×1°spatial resolution and 3-h temporal resolution. The 72-h backward trajectories at a height of 100 m obtained from the National Oceanic and Atmospheric Administration were run every hour. Cluster analysis was performed, and four clusters were determined based on the total spatial variance (TSV) (Chen et al., 2022; Ji et al., 2022).

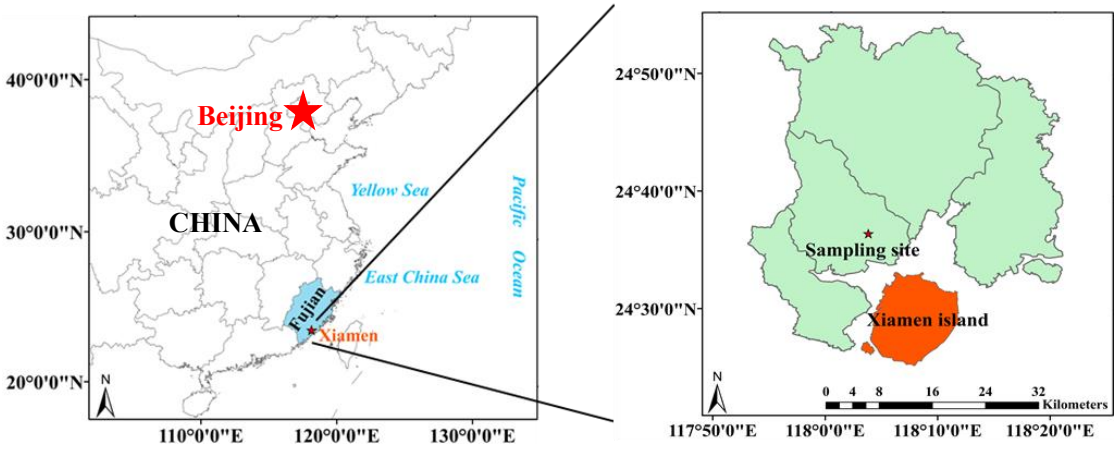

Fig S2. Location of the observation site in a coastal city of Southeast China

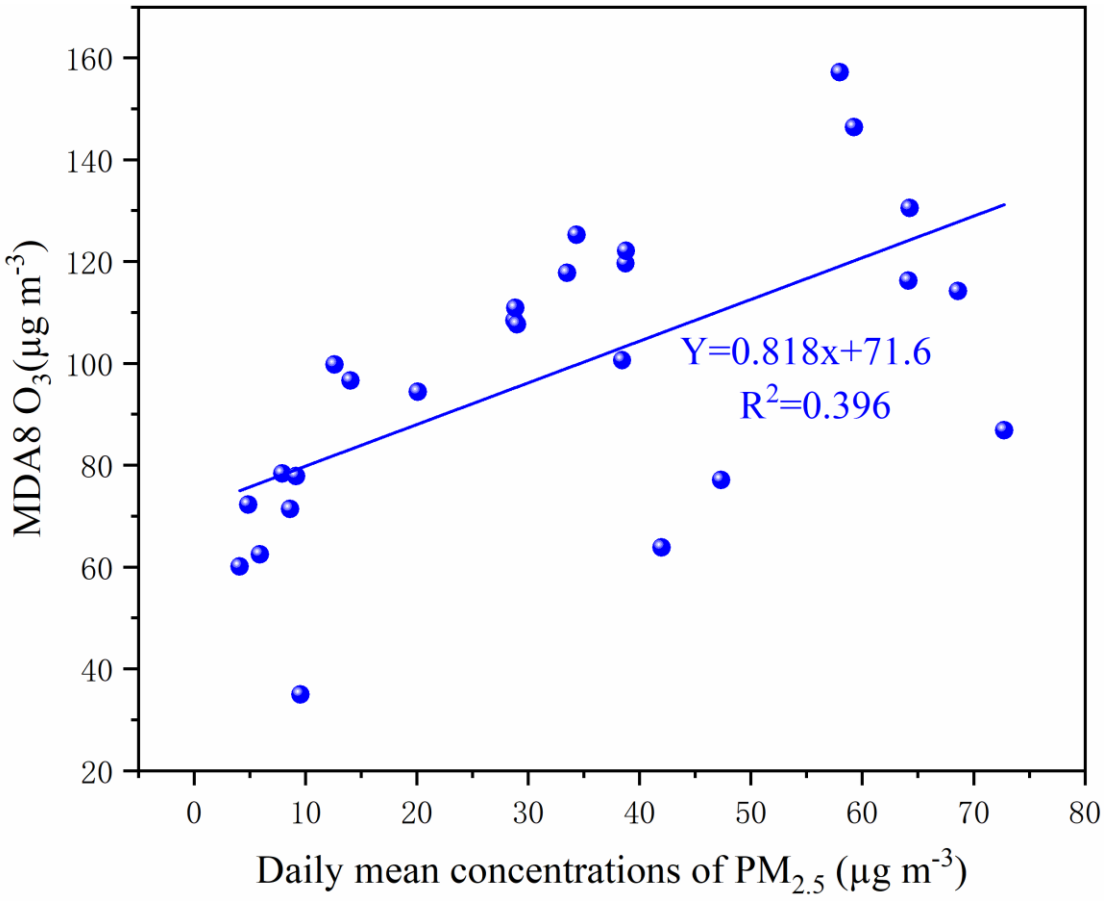

Fig S3. The correlation of $PM_{2.5}$ and MDA8 O3 concentrations during the whole periods

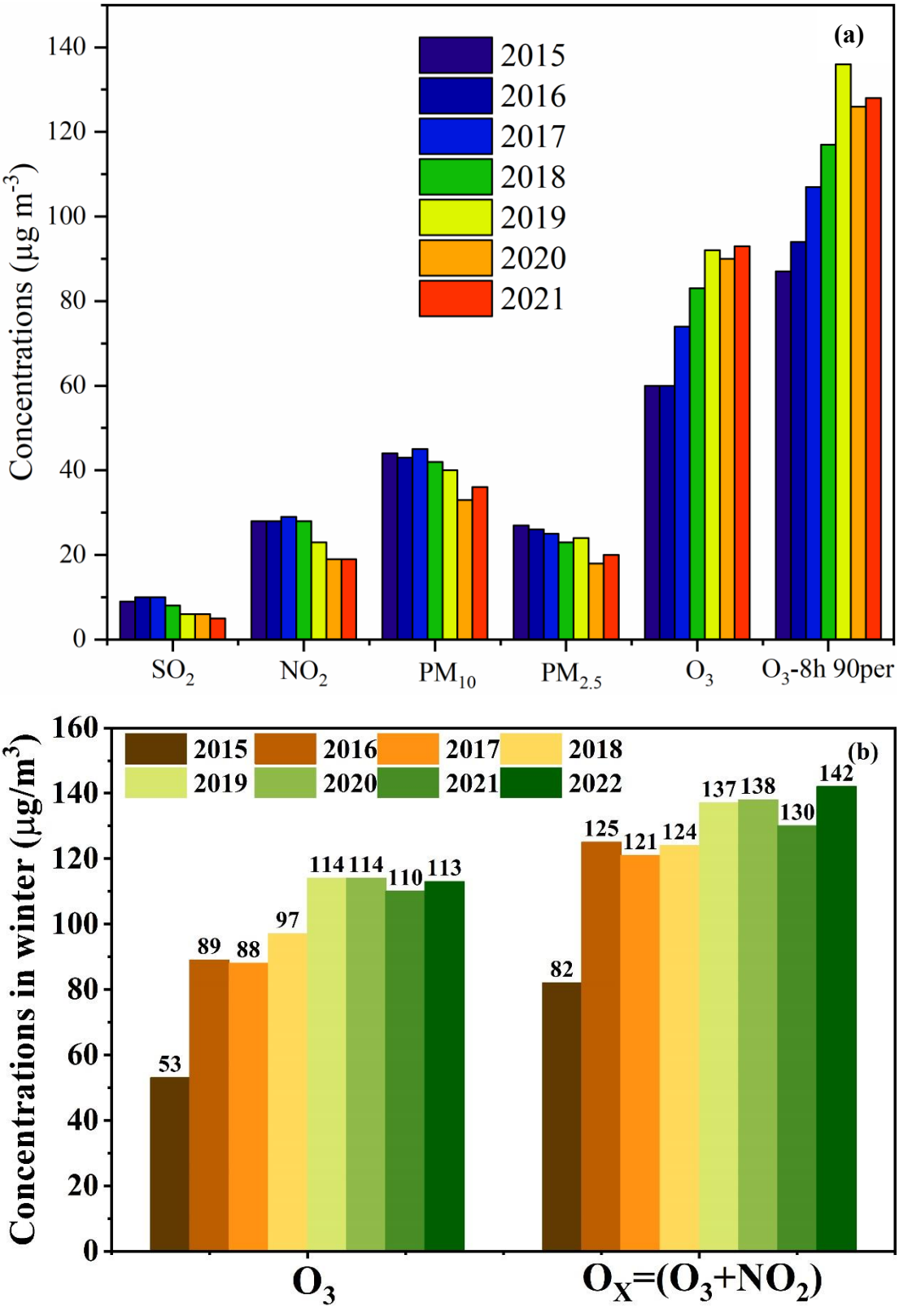

Fig S4. Inter-annual mean concentrations of criteria air pollutants (a) and averaged concentrations of O_3 and Ox in winter in Xiamen, a coastal city of Southeast China

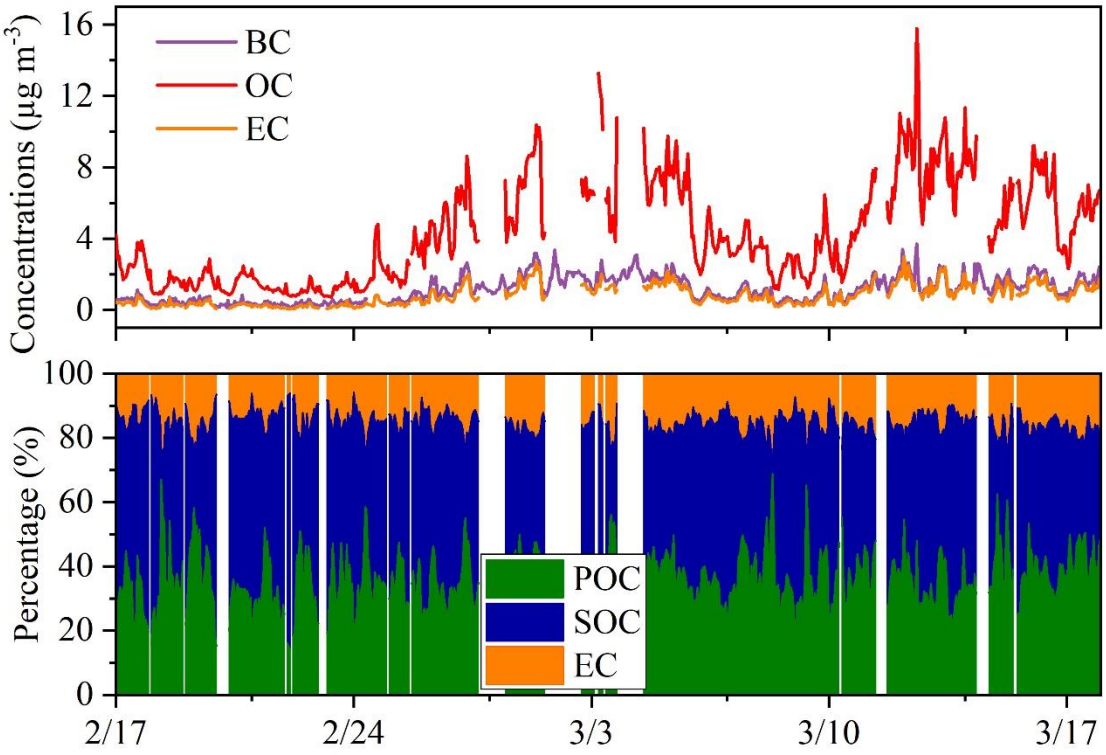

Fig S5. The concentrations and percentages of OC, EC, and BC during the whole periods

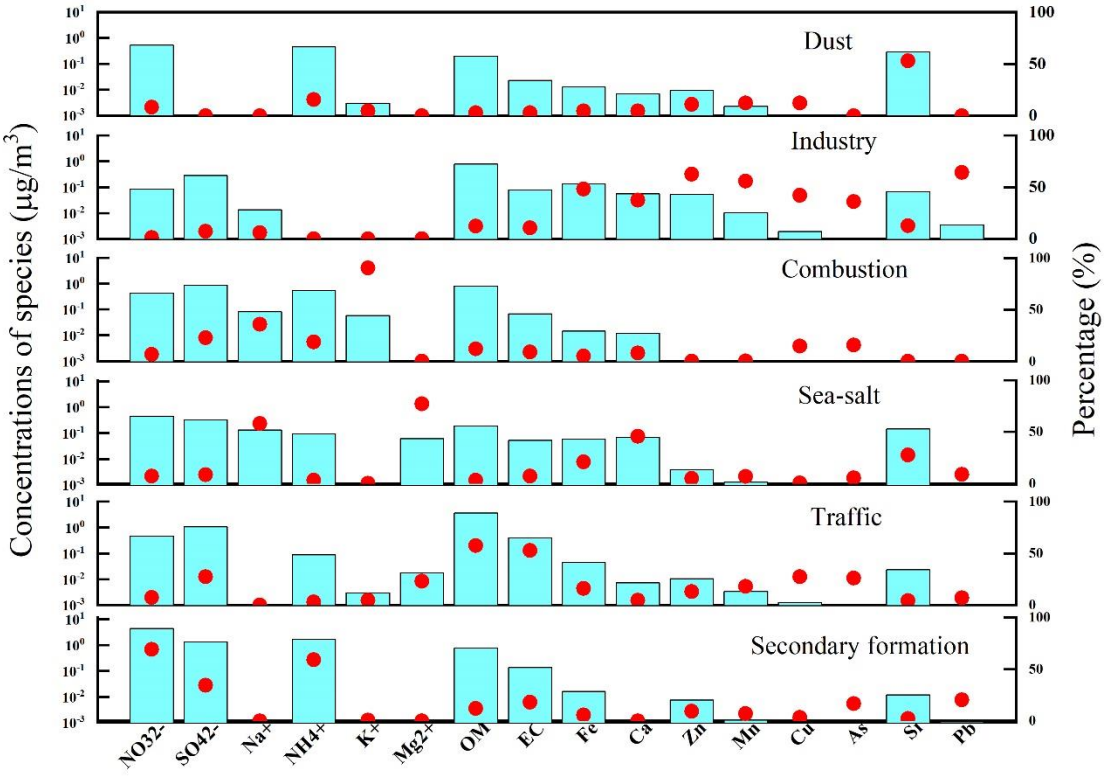

Fig S6. The factor profiles and the contribution of various sources to $PM_{2.5}$ by the positive matrix factorization (PMF) model analysis. The bars represent the concentrations of various species and the dots represent the contributions of species to the factors.

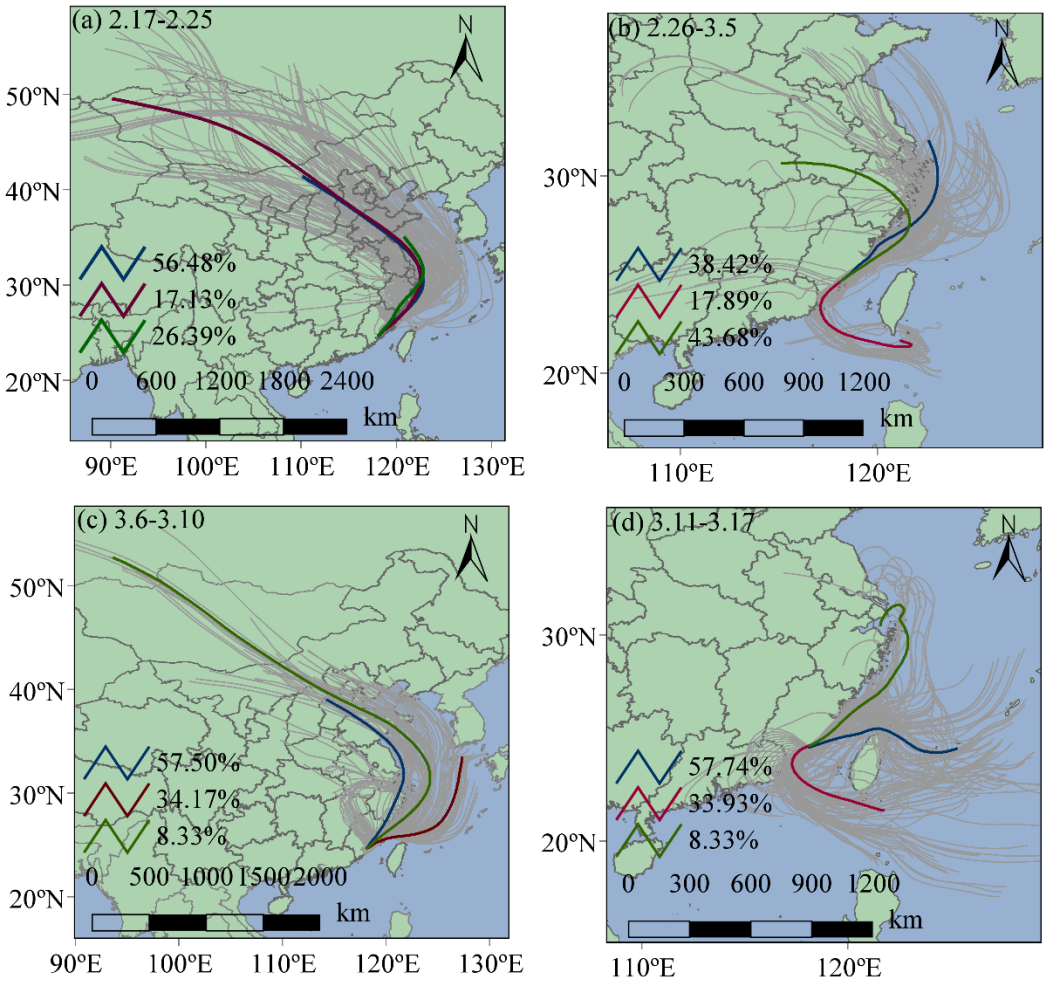

Fig.S7 Backward trajectory clusters at the monitoring site under different periods

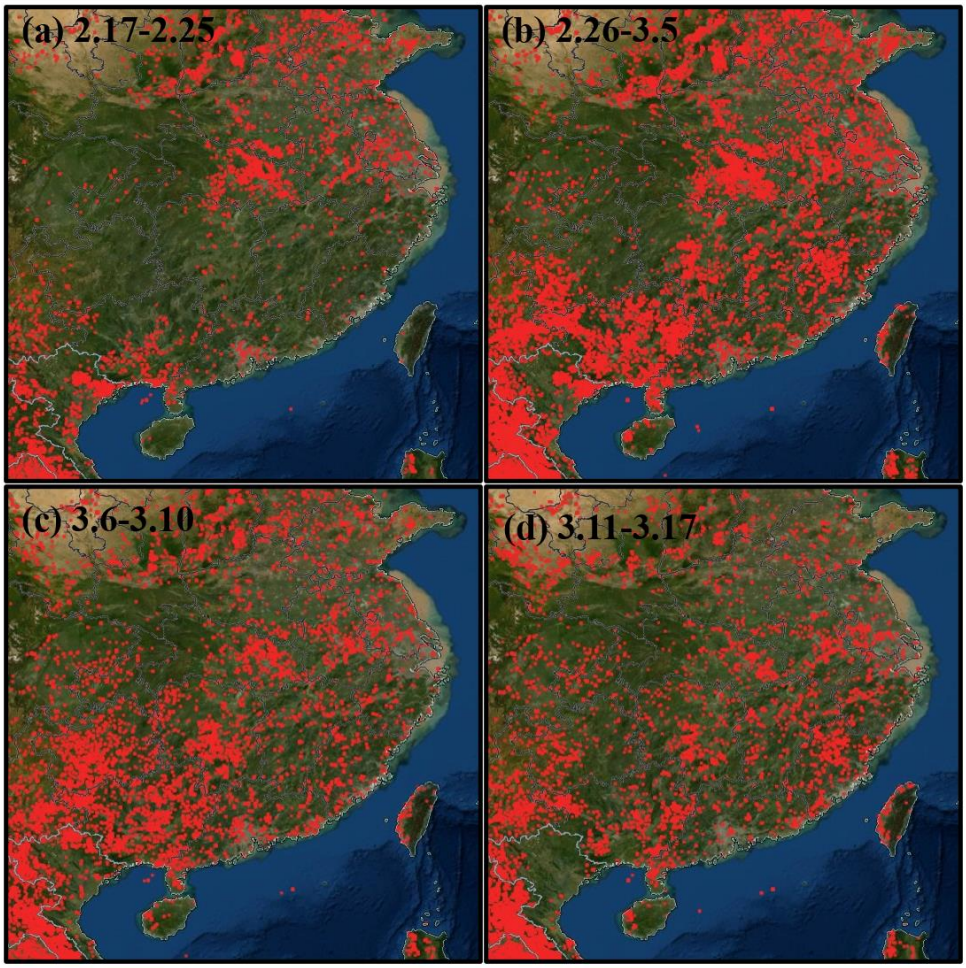

Fig.S8 The distribution of fire spots around the monitoring site under different periods (From the Fire Information for Resource Management System, https://firms.modaps.eosdis.nasa.gov/firemap/)

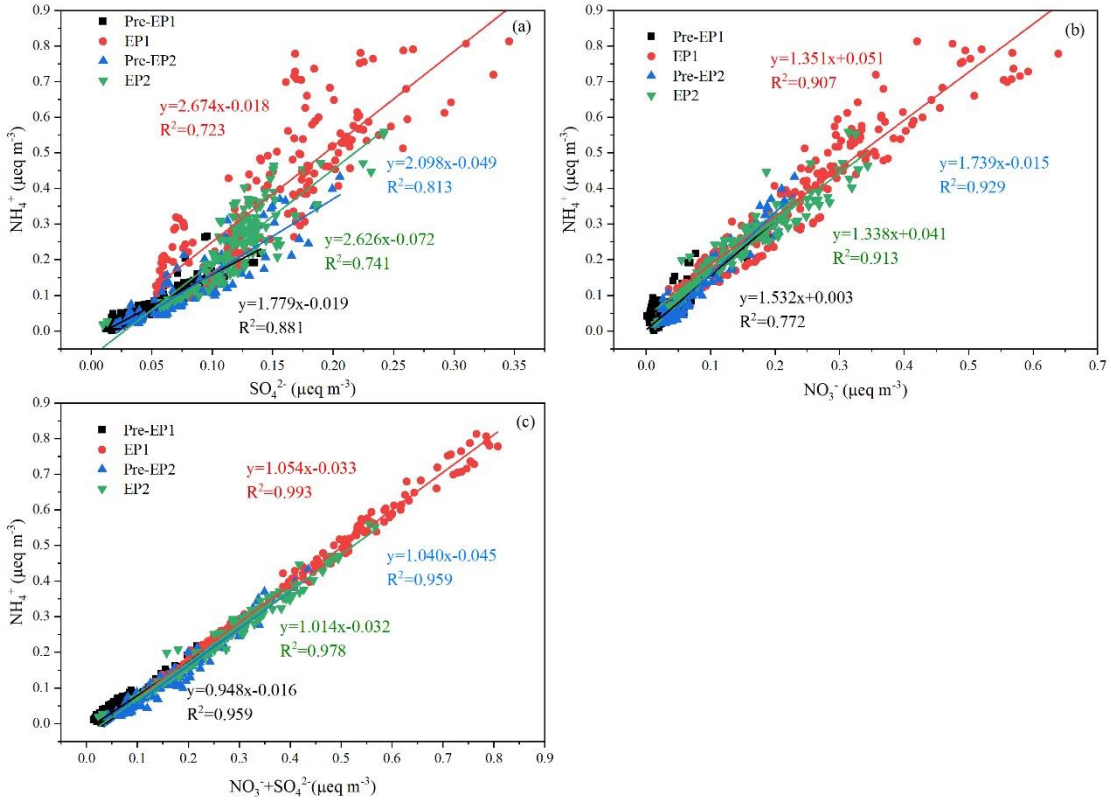

Fig S9.The correlations between (a) NH_4^+ and SO_4^{2-}, (b) NH_4^+ and NO_3^-, and (c) NH_4^+ and $NO_3^-+SO_4^{2-}$

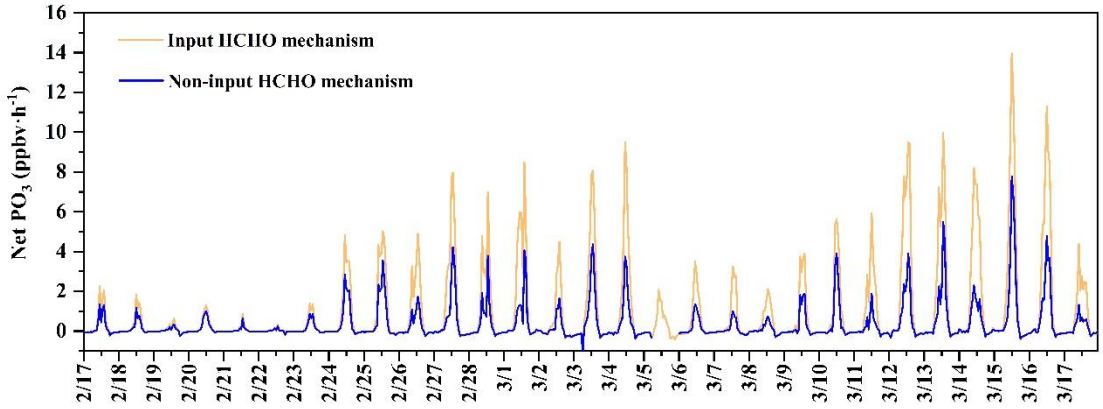

Fig S10. The net O_3 production rates modeled by the OBM with or without HCHO mechanism

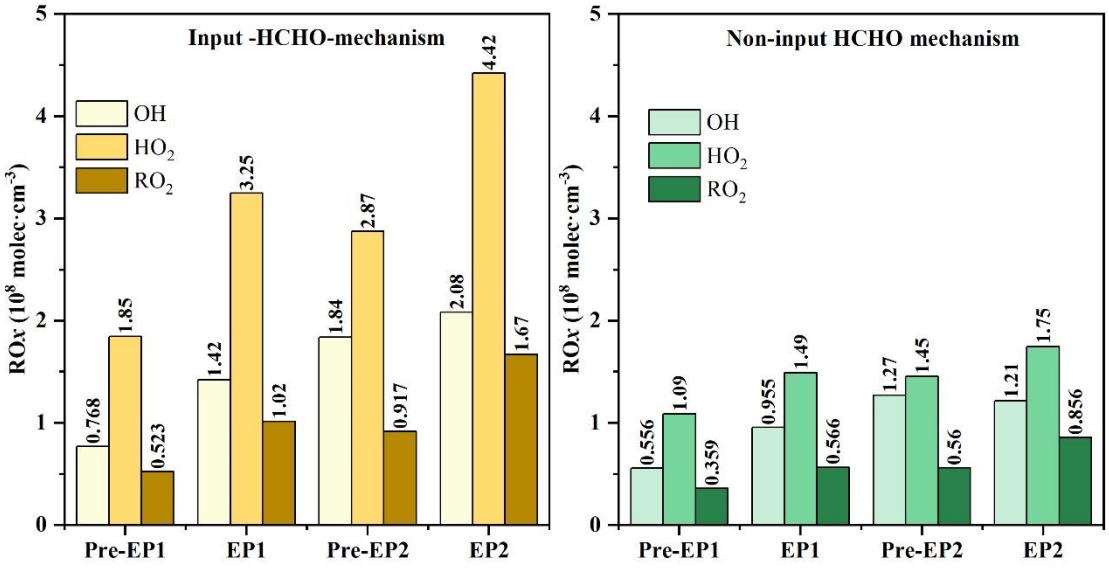

Fig S11. The ROx concentrations modeled by the OBM with or without HCHO mechanism

206

207 Table S1 Mean concentrations of air pollutants, chemical compositions and meteorological
208 parameters under different pollution stages

	Pre-EP1	EP1	Pre-EP2	EP2
$PM_{2.5}$(μg m^{-3})	9.03±6.28	51.94±19.02	33.53±10.41	35.34±23.51
PM_{10}(μg m^{-3})	13.68±10.51	74.43±24.40	57.46±21.11	58.21±28.98
O_3(μg m^{-3})	60.82±18.57	67.12±44.73	76.58±31.83	58.98±47.97
CO(μg m^{-3})	531.02±63.18	742.86±121.34	379.17±95.65	577.98±97.24
SO_2(μg m^{-3})	9.16±3.47	13.74±7.61	16.26±2.68	18.20±6.58
NO_2(μg m^{-3})	12.40±7.00	31.38±14.20	22.01±10.82	32.56±11.08
NO(μg m^{-3})	1.5±1.31	5.56±9.51	2.04±14.29	6.13±8.02
Ox(μg m^{-3})	73.22±12.78	98.50±29.45	88.59±21.32	91.54±29.57
BC(μg m^{-3})	0.45±0.19	1.69±0.56	0.78±0.32	1.61±0.54
OC(μg m^{-3})	1.69±0.81	6.36±2.16	3.20±1.52	7.48±5.03
EC(μg m^{-3})	0.27±0.17	1.23±0.50	0.59±1.51	1.29±0.51
SO_4^{2-}(μg m^{-3})	1.96±1.26	7.07±2.91	3.87±2.24	5.87±1.70
NO_3^-(μg m^{-3})	2.02±1.81	14.95±8.34	4.83±2.83	9.69±4.89
NH_4^+(μg m^{-3})	0.96±0.90	6.77±3.43	2.16±1.63	4.46±1.88
NOR	0.16±0.07	0.32±0.08	0.18±0.06	0.24±0.05
SOR	0.19±0.07	0.38±0.18	0.19±0.06	0.26±0.08
T(℃)	12.38±3.89	20.56±3.90	18.65±4.17	23.93±4.30
RH(%)	69.41±12.45	63.17±10.32	54.30±15.52	62.17±11.05
P(kPa)	101.14±0.36	100.71±0.30	100.68±0.15	100.17±0.21
WS(m/s)	1.64±0.70	1.02±0.51	1.37±0.59	0.93±0.54
UV(W/m^2)	5.88±9.58	9.31±13.94	11.08±16.09	11.10±15.05
JNO_2($\times10^{-3}$ s^{-1})	1.50±2.45	2.49±3.57	2.91±3.94	2.95±3.79
HONO(μg m^{-3})	0.75±0.36	3.10±2.25	1.19±0.58	4.19±2.68
HCHO(ppb)	0.68±0.71	2.94±1.01	1.59±0.71	3.59±1.36
TVOCs(ppb)	14.47±7.14	29.39±11.65	14.28±6.18	29.91±12.05
Aromatics(ppb)	1.29±1.36	3.21±1.92	1.54±1.29	3.06±1.87

Alkynes(ppb)	0.78±0.41	1.04±1.00	0.12±0.06	0.77±0.72
Alkanes(ppb)	6.48±2.06	10.27±5.07	4.46±1.92	9.73±4.46
Alkenes(ppb)	0.75±0.52	1.28±0.84	0.49±0.42	1.37±1.09
OVOCs(ppb)	0.87±0.35	1.21±0.23	1.01±0.41	1.22±0.25
Halohydrocarbon(ppb)	4.30±3.69	12.40±4.77	6.65±3.03	13.76±5.76

209
210
211
212
213

214

215 Table S2 Comparisons of atmospheric HCHO in China

Location	Type	Seasons	Mean(±SD) (ppbv)	Range (ppbv)	Reference
	Urban	Spring	2.9 ± 0.3	0.25-8.34	[12]
Xiamen, China	Urban	Autumn	3.2 ± 1.4	0.38-7.56	[12]
	Urban	Winter	1.95±1.06	0.23-6.22	This study
Shenzhen, China	Urban	Spring	3.4±1.6	N.A.[a]	[2]
Hong Kong, China	Urban	Spring (2012)	3.02±0.91	N.A.	[6]
Shanghai, China	Suburban	Spring (2018)	6.7±3.6	N.A.-20.9	[4]
Shanghai, China	Suburban	Spring (2018)	5.01±3.80	N.A.-18.69	[10]
Beijing, China	Urban	Summer (2013)	11.39±5.58	N.A.	[5]
Shanghai, China	Urban	Summer (2018)	3.31±1.43	N.A.	[8]
Shenzhen, China	Urban	Summer	5.0±4.4	N.A.	[2]
Hong Kong, China	Urban	Summer (2011)	8.07±1.94	N.A.	[6]
Guangzhou, China	Urban	Summer (2010)	6.69±1.98	N.A.	[3]
Yantai, China	Urban	Summer	3.90±1.12	N.A.	[3]
Beijing, China	Suburban	Summer	11.17±5.32	3.14-35.08	[9]
Shanghai, China	Suburban	Summer	2.2±1.8	N.A.-9.4	[7]
Wuhan, China	Suburban	Summer	2.1±0.2	0.6-4.1	[1]
Hong Kong, China	Urban	Autumn (2011)	2.96±0.70	N.A.	[6]
Guangdong,China	Urban	Autumn	4.12±1.02	2.56-7.31	[11]
Beijing, China	Urban	Winter (2013)	7.39±5.26	N.A.	[5]
Shenzhen, China	Urban	Winter	4.2±2.2	N.A.	[2]
Hong Kong, China	Urban	Winter (2012)	2.70±1.20	N.A.	[6]
Guangzhou, China	Urban	Winter	3.35±1.38	N.A.	[3]

216 Note: (a) N.A. means no relevant data available.

217

218

Table S3. The detection limits, time resolutions and measured uncertainties of air pollutants

Species	Measurement Techniques	Uncertainties	Detection limits	Time resolution
HCHO	FMS-100, Focused Photonics Inc., Hangzhou, China	≤5%	50 pptv	1 s
PAN	PANs-1000, Focused Photonics Inc., Hangzhou, China	±10%	50 pptv	5 min
O_3	Model 49i, Thermo Fischer Scientific, USA	±5%	1 ppbv	1 h
NOx	Model 42i, Thermo Fischer Scientific, USA	±10%	0.5 ppbv	1 h
CO	Model 48i, Thermo Fischer Scientific, USA	±5%	40 ppbv	1 h
SO_2	Model 43i, Thermo Fischer Scientific, USA	±10%	0.5 ppbv	1 h
VOCs	GC-FID/MS, TH-300B, Wuhan, China	±10%	20-300 pptv	1 h
HONO	MARGA, ADI 2080, Applikon Analytical B.V., the Netherlands	±20%	50 pptv	1 h

Reference

[1]Zeng P, Lyu X, Guo H, et al. Spatial variation of sources and photochemistry of formaldehyde in Wuhan, Central China[J]. Atmospheric Environment, 2019, 214: 116826.

[2]Wang C, Huang X, Han Y, et al. Sources and Potential Photochemical Roles of Formaldehyde in an Urban Atmosphere in South China[J]. Journal of Geophysical Research: Atmospheres, 2017, 122(21): 11,934-11,947.

[3]Ho K F, Ho S S H, Huang R J, et al. Spatiotemporal distribution of carbonyl compounds in China[J]. Environmental Pollution, 2015, 197: 316-324.

[4]Zhang K. Formation mechanism of HCHO pollution in the suburban Yangtze River Delta region, China: A box model study and policy implementations[J]. Atmospheric Environment, 2021, 267: 118755.

[5]Rao Z, Chen Z, Liang H, et al. Carbonyl compounds over urban Beijing: Concentrations on haze and non-haze days and effects on radical chemistry[J]. Atmospheric Environment, 2016, 124: 207-216.

[6]Cheng Y, Lee S C, Huang Y, et al. Diurnal and seasonal trends of carbonyl compounds in roadside, urban, and suburban environment of Hong Kong[J]. Atmospheric Environment, 2014, 89: 43-51.

[7]Wu Y, Huo J, Yang G, et al. Measurement report: Production and loss of atmospheric formaldehyde at a suburban site of Shanghai in summertime[J]. Atmospheric Chemistry and Physics, 2022, 23: 2997-3014.

[8]Guo Y, Wang S, Zhu J, et al. Atmospheric formaldehyde, glyoxal and their relations to ozone pollution under low- and high-NOx regimes in summertime Shanghai, China[J]. Atmospheric Research, 2021, 258: 105635.

[9]Yang X, Xue L, Wang T, et al. Observations and Explicit Modeling of Summertime Carbonyl Formation in Beijing: Identification of Key Precursor Species and Their Impact on Atmospheric Oxidation Chemistry[J]. Journal of Geophysical Research: Atmospheres, 2018, 123(2): 1426-1440.

[10]Zhang K, Huang L, Li Q, et al. Explicit modeling of isoprene chemical processing in polluted air masses in suburban areas of the Yangtze River Delta region: radical cycling and formation of ozone and formaldehyde[J]. Atmospheric Chemistry and Physics, 2021, 21(8): 5905-5917

[11]Shen H, Liu Y, Zhao M, et al. Significance of carbonyl compounds to photochemical ozone formation in a coastal city (Shantou) in eastern China[J]. Science of The Total Environment, 2021, 764: 144031.

[12]Liu, T., Lin, Y., Chen, J.*, Chen, G., Yang, C., Xu, L., Li, M., Fan, X., Zhang, F., and Hong, Y.* Pollution mechanisms and photochemical effects of atmospheric HCHO in a coastal city of southeast China. Science of the Total Environment. 2023, 859:160210